Journal of Materials Chemistry A

Accepted Manuscript

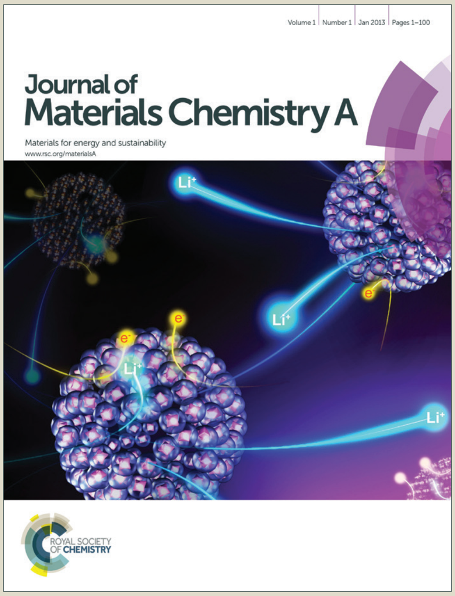

Volume 1 | Number 1 | Jan 2013 | Pages 1–100

Journal of Materials Chemistry A

Materials for energy and sustainability

www.rsc.org/materialsA

ROYAL SOCIETY OF CHEMISTRY

www.rsc.org/materialsA

Journal of Materials
Chemistry A

Dynamic Article Links ▶

Cite this: DOI: 10.1039/c0xx00000x

www.rsc.org/materials

PAPER

Synthesis and electrocatalytic performance of MnO_2-promoted Ag@Pt/MWCNTs electrocatalyst for oxygen reduction reaction

Shuping Yu, Runting Liu, Zhongming Wang, Wensheng Yang, Kefei Han, Hong Zhu*

Two forms of crystalline MnO_2 were synthesized by a hydrothermal method, and MnO_2-doped Ag@Pt/MWCNTs composites were prepared by ultrasonic treatment for oxygen reduction reaction in proton exchange membrane fuel cells (PEMFC). The morphology of the electrocatalyst samples was characterized by X-Ray diffraction (XRD), scanning electron microscopy (SEM) and high resolution transmission electron microscopy (HRTEM). We found that the Ag@Pt/MWCNTs catalyst exhibited a core-shell nanostructure and the two forms of MnO_2 were α-MnO_2 and β-MnO_2. The electrochemical properties of the electrocatalyst samples were studied by cyclic voltammetry (CV), linear sweep voltammetry (LSV), chronoamperometry (CA), and electrochemical impedance spectroscopy (EIS) in acidic medium. The results demonstrated that the Ag10%@Pt10%/MWCNTs-α-$MnO_2$20% had the largest electrochemical activity area (85.83 $m^2 \cdot g^{-1}$) of all electrocatalysts and the oxygen reduction reaction on the electrocatalyst proceeds through the $4e^-$ reduction pathway.

1. Introduction

Efficient oxygen reduction reaction (ORR) is of crucial importance in the field of proton exchange membrane fuel cells (PEMFC)[1-6]. Until now, the most frequently investigated ORR catalysts have been based on noble metals such as Pt and Pt alloys, which have shown the best overall catalytic performance[7-10]. The high cost of the Pt-based catalysts hindered the commercialization of fuel cells. The inter-metallic platinum electrocatalysts with cheap transition metal cores, which reduces the platinum loads and cost, have been studied[11-14]. However, core–shell catalysts usually suffer from disadvantages such as easy poisoning by CO-like intermediate species and the kinetic limitation of the oxygen reduction. Now many studies have focused on the methods to promote the electrochemical durability of core–shell catalysts[15-17].

Recent studies show that metal oxides (e.g., WO_3, MoO_X, Co_3O_4, CeO_2, MnO_2, and SnO_2) have attracted much attention because of their corrosion resistance, spillover, and durability in many catalytic reactions[18-26]. For example, WO_3 can form H_xWO by reacting with hydrogen ions and removing the hydrogen from Pt–H to WO_3, which is known as the spillover effect[27]. Similar phenomena were found by Elezovic et al.[28], who also mentioned that because of the formation of the interface between the platinum and oxides or the surface diffusion of oxygen reaction intermediates, the catalytic activity of MoO_xPt/C was higher than that of Pt/C. Among the other benefits of metal oxides, the chemisorptions of O_2 onto the SnO_2 surface as O^{2-} may be facilitated by Sn^{2+} ions produced by cathode polarization, which plays the determining role at high potentials in oxygen reduction[29]. Yu et al.[25] found that the introduction of CeO_2 to Pt/GN can reduce the CO poisoning effect and promote the methanol electrooxidation. Sundara[30] prepared a carbon nanostructure (CNS) carried over a low cost bi-metal oxide catalyst (Fe-Sn-O) with taking advantage of the strong corrosion resistance of Fe-Sn-O. Furthermore, the oxygen adsorbed on the Fe-Sn-O surface can be converted to OH_{ad} in time. Moreover, the polyvalence of the transitional metal oxides makes them inert to chemical and electrochemical attack under appropriate conditions and exhibit metal-like conductivity.

MnO_2 was known as a promising metal oxide for electrode material because of its low cost, environmental friendliness, and large tunnels. Many previous investigations on MnO_2 focused on ORR catalyst activity, capacitance, and crystal diversity[31-35]. In Na-ion batteries, β-MnO_2 nanorods exhibit better electrochemical performance such as rate capability and cyclability than α-MnO_2 nanorods do because of a more compact (1×1) tunnel structure of β-MnO_2 nanorods for the reversible Na-ion storage[36]. Wang et al.[35] believe that α-MnO_2 nanorods have the highest catalytic activity for ORR because of their crystal phase/morphology in an appropriate oxygen adsorption mode. However, a mechanism for ORR on MnO_2 has not been established because of the complex chemistry between the Mn species. For other studies, Yu et al.[37] prepared a Cu@Pt/MWCNTs-β-MnO_2 composite catalyst that had better catalytic performance and larger electrochemical activity area (up to 71.1 $m^2.g^{-1}$) than Cu@Pt/MWCNTs, with the effect of MnO_2 promoted by a recycle process ($Mn^{4+} \rightarrow Mn^{3+} \rightarrow Mn^{4+}$). Valim et al.[38] revealed that the ORR on the MnO_2 catalysts proceeds preferentially through the complete $4e^-$ reduction pathway via a 2 plus $2e^-$ reduction process involving hydrogen peroxide as an intermediate. Chen et al.[39]prepared a MnO_2@nanoporous gold with large specific capacitance, high cell voltage, small internal resistance, and high energy density.

On the basis of our previous work[40], two forms of crystalline MnO_2 were synthesized byahydrothermal method, and both of them were doped with Ag@Pt/MWCNTs to obtain Ag@Pt/MWCNTs-MnO_2 electrocatalysts. The formation and the morphology of the catalyst were evaluated in this study, where the electrocatalytic properties were estimated by electrochemical measurements.

2. Experimental Section

2.1 Materials

Multi-walled carbon nanotubesnanotubes (MWCNTs) was purchased from Shenzhen Nanotech Port Co., Ltd. Chloroplatinic acid was purchased from Sinopharm Chemical Reagent Co., Ltd. Commercial Pt20%/C catalystwas purchased from Johnson-Matthey (JM). All other chemicals were purchased from the Beijing Chemical Reagent Store (China) and used without further purification. Double-distilled deionized water was used throughout this study.

2.2 Preparation of Ag@Pt/MWCNTs electrocatalyst

Ag@Pt/MWCNTs electrocatalysts (Ag@Pt:C=20:80 by weight) with a core-shell structure were synthesized as previously described[40]. For comparison, Pt20%/MWCNTs catalyst with the same Pt content was synthesized.

2.3 Synthesis of Ag@Pt/MWCNTs-MnO_2 electrocatalyst

First, $KMnO_4$ and $Mn(NO_3)_2$ were first dissolved in 15 mL of deionized water under ultrasound for 2 h. Then the mixture was transferred into a Teflon-lined autoclave. The autoclave was heated to 160 ˚C and kept at 160 ˚C for 8 h, and then brown powder of α-MnO_2 was formed. When the reaction time reached 72 h, β-MnO_2 was formed. The α-MnO_2 and β-MnO_2 were each mixed with Ag@Pt/MWCNTs in ethanol solution under ultrasound to obtain the Ag@Pt/MWCNTs-MnO_2 electrocatalyst. Scheme 1 depicts the synthesis procedure of the Ag@Pt/MWCNTs-MnO_2. The Ag@Pt/MWCNTs was described in a previous study[40]. And the α-MnO_2 and β-MnO_2 were each mixed with Ag@Pt/MWCNTs to obtain Ag@Pt/MWCNTs-MnO_2 electrocatalysts.

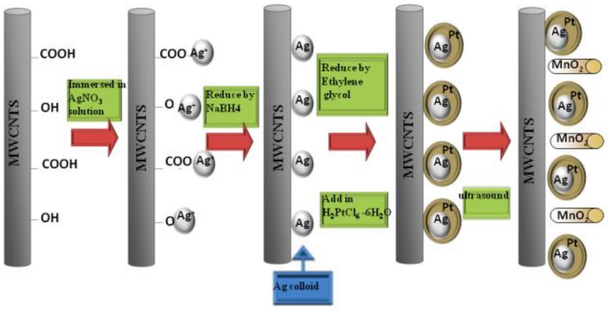

Scheme 1 Schematic diagram for formation of Ag@Pt/MWCNTs-MnO_2 core-shell nanostructure

2.4 Characterization

The morphology of the electrocatalyst was determined by high resolution transmission electron microscopy (HRTEM) on a JEOL S-520 microscope. X-ray diffraction (XRD) analyses were performed on a D/max-2200/PC X-ray diffractometer with a Cu Kα radiation source. The particle size was calculated by using the Scherrer equation:

$$D=0.9\lambda/(B\cos\theta) \qquad (1)$$

where D is the diameter of particle, λ is the X-ray wavelength, θ is the Bragg angle, and B is the full width at half maximum (FWHM, in radians) of the peak under consideration.

Electrochemical measurements were carried out by using a Zahner Ennium electrochemical workstation with a three-electrode cell. 900 µL of ethanol and 100 µL Nafion (5% wt, DuPont) were mixed by ultrasound to form an ink of 5 mg_{catal}/mL. Then, an aliquot of 10 µL of the electrocatalyst ink was transferred to the surface of a glassy carbon disc (5 mm outer diameter) and dried at room temperature. In a typical experiment, a Pt needle and a standard calomel electrode (SCE) were used as the counter-electrode and the reference electrode, respectively. The cyclic voltammetry (CV) tests were conducted at 50 mV s^{-1} in the potential range 0 to 0.3 V (vs. RHE). Then, the electrolyte was purged with O_2 for at least 30 min before linear scan voltammograms (LSV) were obtained. The LSV tests were conducted at 5 mV s^{-1} in the potential range 0.1 to 0.8 V (vs. SCE) at different rotating speeds (100, 400, 900, 1600 and 2500 rpm).

3. Results and discussion

3.1 Physicochemical Studies

The XRD patterns of the Pt/MWCNTs and Ag@Pt/MWCNTs electrocatalysts recorded in the 2θ range of 10°-90 ° are shown in Fig.1**.** The diffraction peaks of Ag is not obvious in the pattern of Ag@Pt/MWCNTs, an indication that the Ag in Ag@Pt is mostly wrapped by Pt. Compared with the characteristic diffractions peaks of Pt/MWCNTs, the diffractions peaks of Ag@Pt/MWCNT (Fig.1 (B)) has a negative shift. This implies that the Pt lattice has expanded to cover the Ag to form an Ag@Pt structure. The size of Ag@Pt/MWCNTs was estimated to be 8 nm according to the Scherrer equation.

Fig.2 presents the XRD patterns of the different crystalline forms of MnO_2. The characteristic diffraction peaks for the different forms of MnO_2 are clear, and no noise peak can be seen. The XRD pattern in Fig.2 (A) corresponds to a tetragonal phase of β-MnO_2 (JCPDS No. 24-0735) with the lattice constants of a = 0.4399 nm and c = 0.2874 nm. All the reflections in Fig.2 (B) can be indexed to a pure tetragonal phase of α-MnO_2 (ICDD-JCPDS No. 44-0141) with the lattice constants of a = 0.9784 nm and c = 0.2863 nm. The crystal structure of MnO_2 is expected to affect the electrochemical properties.

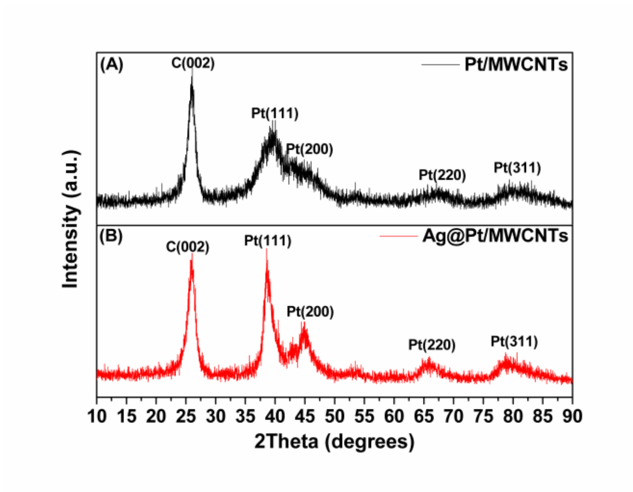

Fig. 1 XRD patterns of different electrocatalysts: (A) Pt/MWCNTs; (B) Ag@Pt/MWCNTs.

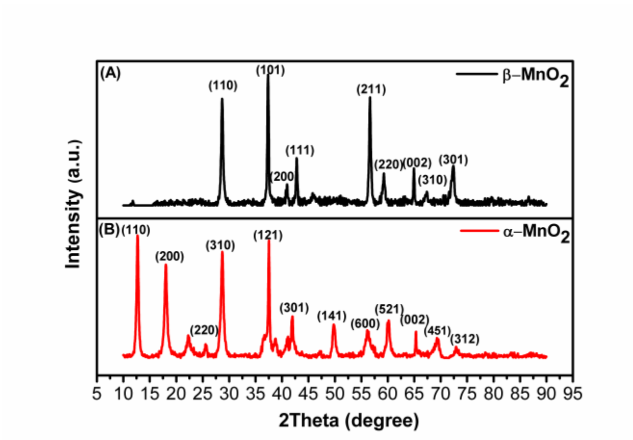

Fig. 2 XRD patterns of different crystalline forms of MnO_2: (A) β-MnO_2; (B) α-MnO_2.

Fig.3 is the images of the electrocatalys. Fig.3 (A) shows that the Ag@Pt particles with an average diameter of about 8 nm were uniformly dispersed on the MWCNT support. The core-shell structure of Ag@Pt is observed in Fig.3 (B). The lattice spacing of the Ag crystalline (111) plane is 0.236 nm, while the lattice spacing of the Pt crystalline (111) plane is 0.228 nm. The SEM of Ag@Pt/MWCNT is shown in Fig.3 (C) as comparison. The SEM images of α-MnO_2 and β-MnO_2 are shown in Fig.3 (D-E).Fig.3 (D) shows that β-MnO_2 is 1.5 μm in diameter and 4-6 μm in length and Fig.3 (E) shows that α-MnO_2 is 20-40 nm in diameter and 2-4 μm in length. α-MnO_2 can be transformed into β-MnO by extending the heating time. Fig.3 (F) and Fig.3 (G) are the composite morphology of the Ag@Pt/MWCNT-α-MnO_2 and Ag@Pt/MWCNT-β-MnO_2. The MnO_2 insert into Ag@Pt/MWCNT formed a uniform structure.

3.2 Electrochemical tests

Fig. 4 shows the CV of the electrocatalysts with different Ag:Pt weight ratios and Pt20%/C (JM). According to Fig. 4, Electrochemically active area (EAS) and Mass specific activity (MSA) of all catalysts are shown in Table 1. Both EAS and MSA of Ag10%@Pt10%/MWCNTs (EAS: 66.15 m^2 g^{-1} and MSA 66.08mA/mg•Pt) are higher than those of Pt20%MWCNT (EAS: 45.88 m^2 g^{-1} and MSA 44.31 mA/mg•Pt), indicating that the catalytic activity and utilization of per unit Pt are better for Ag10%@Pt10%/MWCNTs than for Pt20%MWCNT, though H_2 desorption peak of Pt20%/MWCNTs is larger than Ag10%@Pt10%/MWCNTs. Then this paper will choose the Ag10%@Pt10%/MWCNTs to dope with MnO_2 and study the catalytic activity and mechanism of the composite materials.

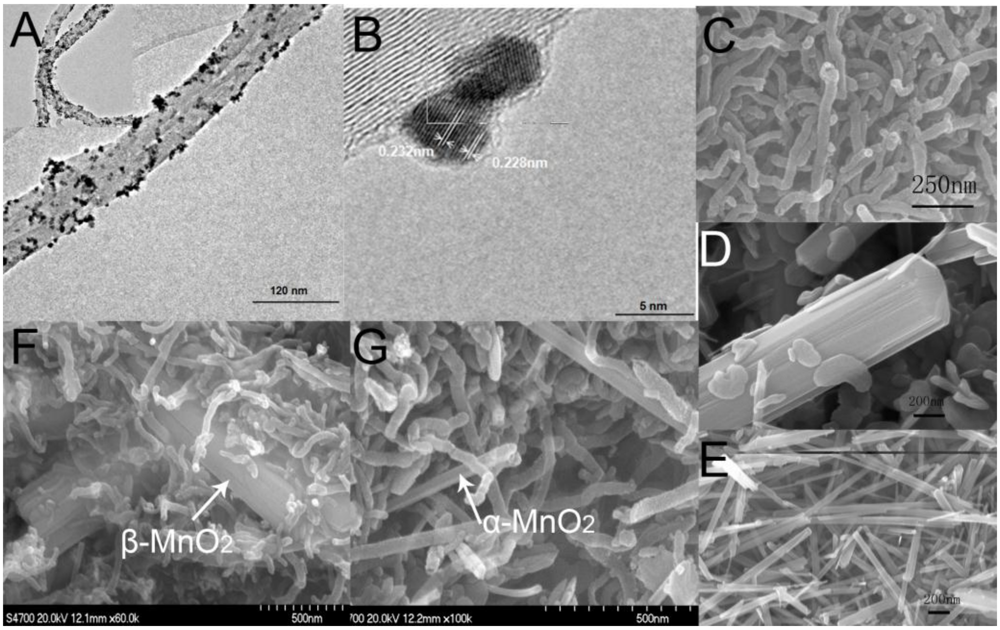

Fig. 3 The images of electrocatalyst: (A) HRTEM image of Ag@Pt/MWCNTs; (B) HRTEM image of Ag@Pt nanoparticles. **(C)** SEM image of Ag@Pt/MWCNTs (D) SEM image of β-MnO_2 (E) SEM image of α-MnO_2, (F) SEM image of Ag@Pt/MWCNT-β-MnO_2 and (G) SEM image of Ag@Pt/MWCNT-α-MnO_2.

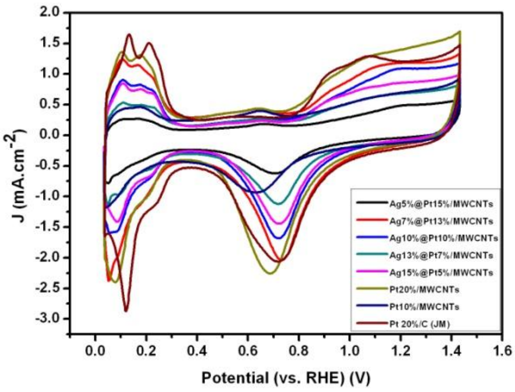

Fig. 4. Cyclic voltammograms of electrocatalysts with different Ag:Pt mass ratios. Electrolyste: 0.5 mol·L^{-1} H_2SO_4. Scanning speed: 50 mV·s^{-1}

Table 1 EAS, and MSA of Ag@Pt/MWCNTs electrocatalyst.

Catalysts	Metal loading (wt%)		EAS(m^2/ g • Pt)	MSA*(mA/ mg • Pt)
	Pt	Ag		
Ag@Pt/MWCNTs	10	0	26.97	11.87
	20	0	45.88	44.31
	15	5	38.67	37.81
	13	7	62.37	61.11
	10	10	66.15	66.08
	7	13	53.87	62.94
	5	15	44.90	49.16
Pt/C (JM)	20	--	51.59	40.46

*. Mass specific activity of platinum around the peak potential (0.7 V vs. RHE) of oxygen reduction

The CV of Ag10%@Pt10%/MWCNTs doped with different crystalline forms of MnO_2 are shown in Fig.5. When the doping proportion of MnO_2 is 20%, the MnO_2-doped electrocatalysts performs the best electrochemical property than the other doping proportions. The corresponding EAS of the Fig.6 is shown in Table 2. The EAS of Ag10%@Pt10%/MWCNTs-β-$MnO_2$20% (68.83 m^2 g^{-1}) and Ag10%@Pt10%/MWCNTs-α-$MnO_2$20% (85.83 m^2 g^{-1}) are both higher than that of Ag10%@Pt10%/MWCNTs (66.15 m^2 g^{-1}) and Pt20%/C (JM) catalyst (51.59 m^2 g^{-1}). It suggests that doping of MnO_2 can promote the electrical properties of Ag10%@Pt10%/MWCNTs. But doping of excessive MnO_2obstructed the active site of Pt, which leads to a decrease of the accessibility of O_2 to the surface of Pt[41].

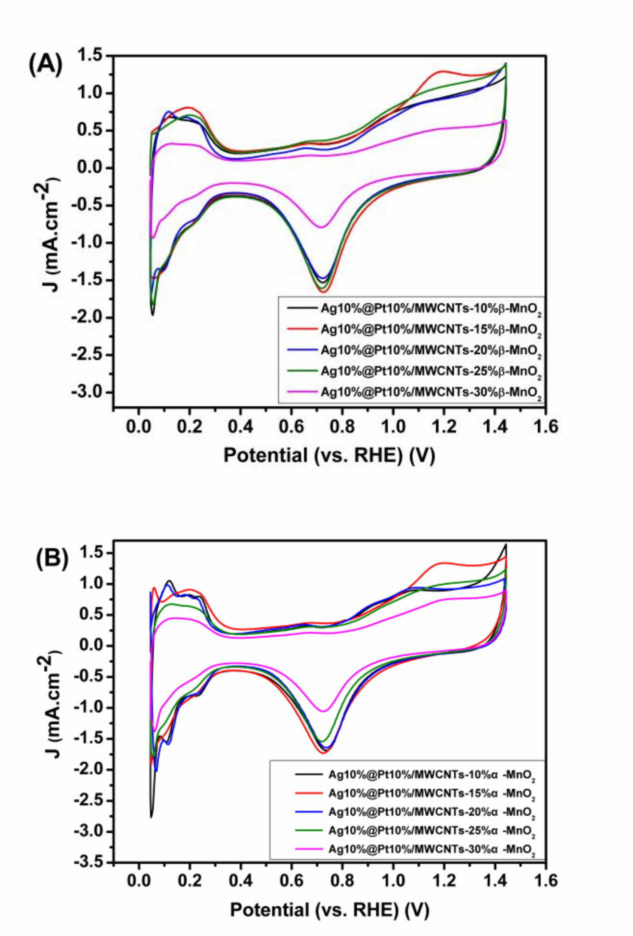

Fig. 5 Cyclic voltammograms of Ag10%@Pt10%/MWCNTs-MnO_2 with different forms of MnO_2. Electrolyte: 0.5 mol·L^{-1} H_2SO_4. Scanning speed: 50 mV·s^{-1}

Table 2 EAS of 10%Ag@10%Pt/MWCNTs doped with different forms of MnO_2

Catalysts	Metal loading (wt %)		MnO_2 doping amount (wt %)	EAS (m^2 g^{-1})
	Pt	Ag		
Ag@Pt/ MWCNTs-β-MnO_2	10	10	0	66.15
			10	63.82
			15	67.07
			20	68.83
			25	65.10
			30	40.57
Ag@Pt/ MWCNTs-α-MnO_2	10	10	10	65.58
			15	72.16
			20	85.83
			25	74.12
			30	46.51

Fig.6 shows the polarization curves of Ag10%@Pt10%/MWCNTs, Pt20%/C (JM), Ag10%@Pt10%/MWCNTs-β-$MnO_2$20% and Ag10%@Pt10%/MWCNTs-α-$MnO_2$20%. The onset reduction potential of electrocatalysts doped with β-MnO_2 (0.975 V) and α-MnO_2 (0.985 V) shifts 40mV and 50 mV, towards positive potentials with respect to the corresponding Ag@Pt/MWCNTs (0.935 V) respectively. Moreover, the onset reduction potential of MnO_2 doped electrocatalysts shifts 20 mV and 30mV towards positive potentials with respect to the Pt20%/C (JM) (0.955 V) catalyst respectively.

The improved ORR activity may be due to the dynamic spillover of surface oxide, as described in the literature[27,42].The oxygenated Pt species (Pt-OH species) on the surface of Ag@Pt/MWCNTs-MnO_2 was easily transferred to MnO_2 by spillover. Furthermore, MnO_2 can promote the reduction of oxygen. H^+ combines with the O^{2-}in MnO_2 to form MnOOH, which can be reduced to O_2 and substantially speeds up the ORR[37].

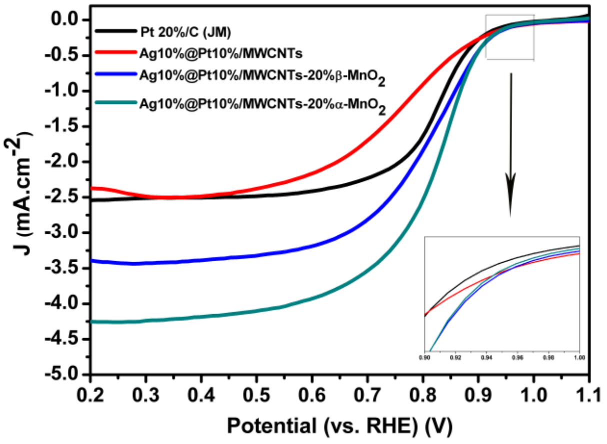

Fig. 6 Polarization curves of different electrocatalysts: Pt20%/C (JM), Ag10%@Pt10%/MWCNTs, Ag10%@Pt10%/MWCNTs-β-$MnO_2$20%, and Ag10%@Pt10%/MWCNTs-α-$MnO_2$20%. Electrolyte: O_2-saturated 0.5 mol·L^{-1} H_2SO_4. Sweep rate: 5 mV·s^{-1}. Rotation speed: 1600 rpm.

The $4e^-$ reduction pathway is preferred in the ORR because of its high catalytic efficiency for PEMFC[37, 43, 44] Thus, the number of transferred electrons in the ORR is an important parameter to evaluate the catalytic performance. The polarization curves at different rotation rates are shown in Fig.7 A(1), A(2), and A(3). The corresponding Koutecky-Levich (K-L) curves of the electrocatalysts at different potentials are shown in Fig.7 B(1), B(2), and B(3). The data for the K-L curves were calculated according to Eq. (2):

$$J^{-1}=J_k^{-1}+(0.62nFD^{2/3}C\mu^{-1/6}w^{1/2})^{-1} \qquad (2)$$

where J and J_k are the measured kinetic current densities of the electrocatalyst, n is the total number of electrons transferred, F is the Faraday constant, D is the diffusion coefficient of oxygen, C is the saturated concentration of oxygen in 0.5 mol·L^{-1} H_2SO_4, μ is the kinetic viscosity of O_2 saturated, and w is the rotation rate. The calculated values of n of the K-L curves are presented in Table 3. It is clear that the n of MnO_2-doped electrocatalyst is higher than those for then non-MnO_2-doped electrocatalysts over the entire potential range. In particular, the n of α-MnO_2-doped electrocatalyst is nearly 4, indicating that α-MnO_2 has the most efficient promoted catalytic effect to ORR. First, MnO_2 is in part determined by the reversible adsorption/desorption of reactants/products into and out of the open tunnel structure.The adsorbed oxygen can be accommodated in the (1×1) tunnels via the bridge mode, therefore the kinetics for oxygen reduction can be enhanced. Since α-MnO_2 has both (2×2) and (1×1) tunnels surrounded by double binding octahedral chains[44], protons can be inserted easily into the α-MnO_2 tunnel structure to form MnOOH. Secondly, the α-MnO_2-doped electrocatalyst has a large surface area and great gathering of MnOOH.Therefore the α-MnO_2 doped electrocatalysts indicates a greater ability to speed up the ORR than non-MnO_2-doped electrocatalysts.

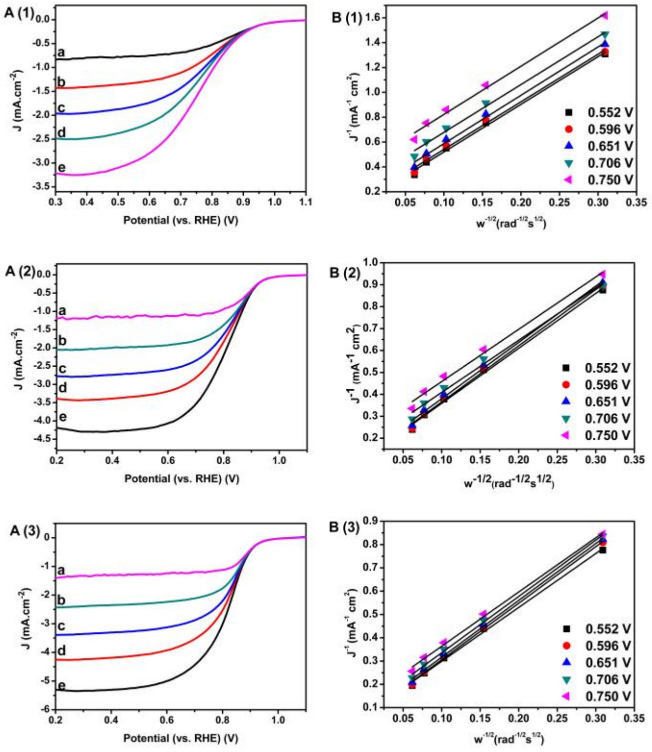

Fig. 7 (A) Polarization curves of A(1): Ag10%@Pt10%/MWCNTs, A(2): Ag10%@Pt10%/MWCNTs-β-$MnO_2$20% and A(3): Ag10%@Pt10%/MWCNTs-α-$MnO_2$20% at different rotation rates: a, 100r/min; b, 400r/min; c, 900r/min; d, 1600r/min; and e, 2500r/min. **Fig.7 (B)** Corresponding K-L curves to Fig.8 (A); Electrolyte: O_2-saturated 0.5 mol·L^{-1} H_2SO_4. Sweep rate: 5mV·s^{-1}. Rotation speed: 1600 rpm.

Table 3. Number of transferred electrons for various catalysts at various potentials

Catalysts	Potential (V)	Corresponding K-L curves	n*
Ag10%@Pt10 %/MWCNTs	0.552	y = 3.833x + 0.136, R ²= 0.996	2.36
	0.596	y = 3.829x + 0.158, R ²= 0.996	2.37
	0.651	y = 3.889x + 0.198, R ²= 0.996	2.33
	0.706	y = 3.845x + 0.293, R ²= 0.996	2.34
	0.750	y = 3.878x + 0.434, R ²= 0.995	2.34
Ag10%@Pt10 %/MWCNTs-β-$MnO_2$20%	0.552	y = 2.508x + 0.108, R ²= 0.996	3.61
	0.596	y = 2.561x + 0.109, R ²= 0.996	3.54
	0.651	y = 2.566x + 0.123, R ²= 0.996	3.53
	0.706	y = 2.380x + 0.170, R ²= 0.996	3.80
	0.750	y = 2.385x + 0.219, R ²= 0.996	3.79
Ag10%@Pt10 %/MWCNTs-α-$MnO_2$20%	0.552	y = 2.312x + 0.067, R ²= 0.997	4.00
	0.596	y = 2.426x + 0.063, R ²= 0.998	3.73
	0.651	y = 2.438x + 0.072, R ²= 0.998	3.73
	0.706	y = 2.416x + 0.094, R ²= 0.999	3.76
	0.750	y = 2.327x + 0.130, R ²= 0.997	3.90

*: Number of transferred electrons

The above results of CV and LSV can be further confirmed by the electron transfer results of different electrocatalysts (as presented in Fig.8). Fig.8 shows that the resistance performance decreases because of the mass transport limitations placed by the increase of the diameter of the arc in the Nyquist plots for Pt20%/C (JM), Ag10%@Pt10%/MWCNTs and Ag10%@Pt10%/MWCNTs-β-$MnO_2$20%. The corresponding diameter for Ag10%@Pt10%/MWCNTs-α-$MnO_2$20% is significantly smaller. This smaller diameter implies that α-MnO_2 facilitates the transport of electrons to react with oxygen, thus making the catalyst active surface more accessible. Moreover, α-MnO_2 has wider tunnels than β-MnO_2. The tunnels are available for the adsorption of oxygen which directly reduces the mass-transfer resistance from water to the surface of the catalyst.

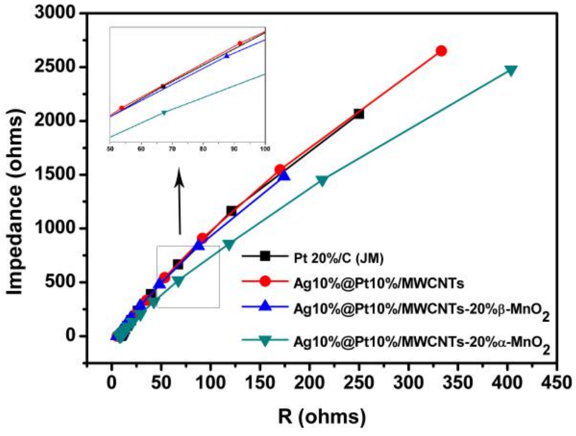

Fig.8 Nyquist plots of different electrocatalysts: Pt20%/C (JM),Ag10%@Pt10%/MWCNTs, Ag10%@Pt10%/MWCNTs-β-$MnO_2$20% and Ag10%@Pt10%/MWCNTs-α-$MnO_2$20%. Electrolyte: 0.5 mol·L^{-1} H_2SO_4,Frequency scan: 0.1-1×10^5Hz.

Furthermore， to evaluate the activity and stability of the electrocatalysts, their chronoamperometry curves at the applied voltages 0.535 V, 0.635 V, and 0.735 V are shown in Fig.9. The steady current of Ag10%@Pt10%/MWCNTs-α-$MnO_2$20% is the highest of the four electrocatalysts at all of the applied voltages, an indication that the core-shell structure and the existence of MnO_2 have effectively improved the electrocatalytic activity of the Ag10%@Pt10%/MWCNTs electrocatalyst, in agreement with the results of cyclic voltammetry.

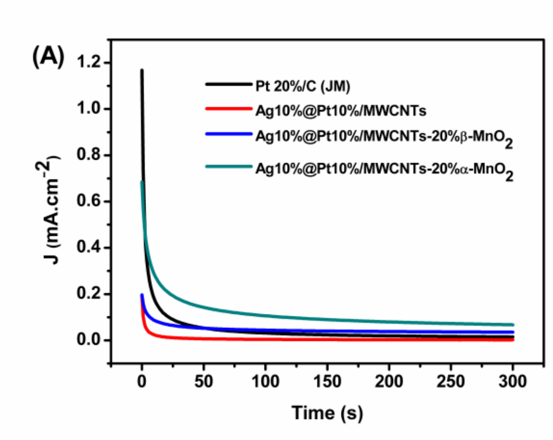

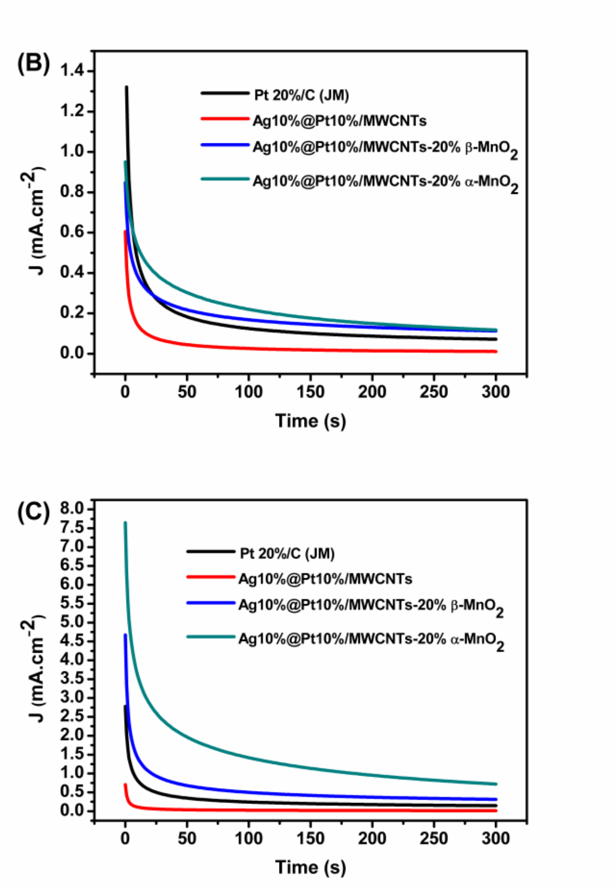

Fig.9 Chronoamperometry curves at different applied voltages ((A) 0.535 V, (B) 0.635 V, and (C) 0.735V) for different electrocatalysts: Pt20%/C (JM), Ag10%@Pt10%/MWCNTs, Ag10%@Pt10%/MWCNTs-β-$MnO_2$20% and Ag10%@Pt10%/MWCNTs-α-$MnO_2$20%. Electrolyte: 0.5 mol·L^{-1} H_2SO_4. Scanning speed: 50 mV·s^{-1}

The mechanism of ORR on MnO_2-doped Ag@Pt/MWCNTs is summarized in Scheme 2. O_2 formed by a two-electron $\sigma(3\sigma_g)^2$ bond and two three-electron $\pi(1\pi_u)^2(\pi_g)^1$ bond. The π bond are easily broken andformed a σ-type bondon the surface of Pt in the O_2-saturated electrolyte: σ orbital of O_2 donates electron density to an acceptor $d_z{}^2$ orbital on Pt (scheme2a,b). Subsequently, the 2p oribital accepts e^- and H^+ forming OH_{ads} and adsorbed on the surface of Pt[45, 46] (PtOH, scheme2c). But the adsorbed OH_{ads} will hinder the further adsorption of O_2. With the introduction of the Ag core, part of the Pt is replaced by Ag, then the oxygenated Pt specieshave a weaker adsorption energy on the Ptthan Ag and part of the OH_{ads} transferred onto the surface of Ag[47] (scheme2d).After Ag@Pt/MWCNTs is doped with MnO_2, for one thing, Mnand the oxygenated Pt species forms Mn-O-Pt bonds and because of the d orbitals of Mn has stronger electron acceptance ability than Pt, the oxygenated Pt species transferred to MnO_2, then convert to OH_{ad} in time (scheme2e). For another thing, MnO_2 forms MnOOH in acid($MnO_2 + H^+ + e^- \rightarrow MnOOH$),and the O_2 chemisorbed onto the MnOOH surface will be reduced to H_2O($MnOOH + 1/2O_2 + e^- + H^+ \rightarrow MnO_2 + H_2O$, scheme2f)[48]. Pt loses -OH to promote oxygen adsorption,then the ORR on the catalysts proceeds preferentially through thecomplete $4e^-$ reduction pathway involving H_2O as an product (as shown in

Fig.6). Thus, the synergic effect between MnO_2 and Ag@Pt enhances the transport of electrons and promotes the catalytic efficiency for ORR.

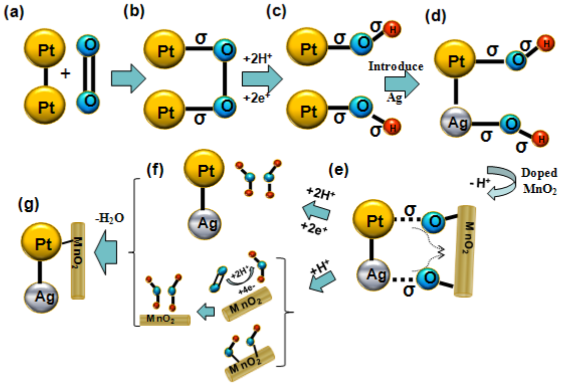

Scheme 2 Schematic diagram for mechanism of ORR on Ag@Pt/MWCNTs-MnO_2 core-shell nanostructure

4. Conclusions

Two forms of crystalline MnO_2 were synthesized by ahydrothermal method, and MnO_2-doped Ag@Pt/MWCNTs composites were prepared by ultrasonic treatment for oxygen reduction reaction in proton exchange membrane fuel cells (PEMFC).

The morphology of MnO_2 was characterized by SEM, XRD and HRTEM. The MnO_2-doped electrocatalysts showed better kinetic behavior as an inexpensive electrocatalyst for oxygen reduction reaction than Ag@Pt/MWCNTs. Particularly, the α-MnO_2 nanorods appear to have the highest catalytic activity and stability because of their crystal phase/morphology in an appropriate oxygen adsorption mode, and the EAS (85.83 $m^2\ g^{-1}$) of the Ag10%@Pt10%/MWCNTs-α-$MnO_2$20% is the highest of all the electrocatalysts in this work. The ORR on the MnO_2-doped catalysts proceeds preferentially through the complete $4e^-$ reduction pathway.

Acknowledgements

The financial supports from the National Natural Science Foundation of China (No. 21176022, 21176023, 21276021 and 21376022), the International S&T Cooperation Program of China (No. 2013DFA51860), the National High Technology Research and Development Program of China (No. 2011AA11A273), Program for Changjiang Scholars and Innovative Research Team in University （IRT1205） are gratefully acknowledged.

Notes and references

State Key Laboratory of Chemical Resource Engineering, Beijing University ofChemical Technology, School of Science, Beijing 100029, China
China. E-mail: zhuho128@126.com

1. G. Evgeniy, A. Zinovieva, N. Voropaev, A. Simonov, V. Romanenko, and G. Okunev,*Int. J. Hydrogen Energy*, 2012,**37**,11894-11903.
2. W. Chao, M. Markovic, and V. Stamenkovic, *ACS. Catal.*, 2012, 2, 891-898.
3. K. Christopher, E. Scofield, H. Liu, and S. Wong, *J. Phys. Chem. Lett.*, 2012, 3, 3385-3398.
4. Y. Daijun, B. Li, H. Zhang, and J. Ma,*Int.J. Hydrogen Energy*, 2012, 37, 2447-2454.
5. D. Laetitia, M. Lopez-Haro, L. Castanheira, J. Durst, M. Chatenet, P. Bayle-Guillemaud, L. Guétaz, N. Caqué, E. Rossinot, and F. Maillard, *Appl. Catal. B*, 2013, 142, 801-808.
6. S. Lyons, and A. Campbell,*J. Phys. Chem. Lett.*, 2013, 4, 393-401.
7. C. Siguo, Z. Wei, X. Qi, L. Dong, Y. Guo, L. Wan and Z. Shao, *J. Am. Chem. Soc.*, 2012, 134, 13252-13255.
8. L. Ying,and E. Mustain, *J. Am. Chem. Soc.*, 2012, 135, 530-533.
9. Y. Lijun, B. Vukmirovic, D. Su, K. Sasaki, A. Herron, M. Mavrikakis, S. Liao, and R. Adzic,*J. Phys. Chem. C*, 2012, 117, 1748-1753.
10. P. Nathan, H. Wu, Z. Quan, and J. Fang, *Acc. Chem. Res.*, 2013.
11. Z. Nan and Y. Xu, *Chem. Mater.*, 2013, 25, 1979-1988.
12. M.Kettner, B. Schneider, and A. Auer, *J. Phys. Chem. C*, 2012, 116, 15432-15438.
13. G. Chaudhuri, and S. Paria, *Chem. Rev.*, 2011, 112, 2373-2433.
14. M. Vismadeb, M. Chi, L. More, and S. Sun, *J. Am. Chem. Soc.*, 2010, 132, 7848-7849.
15. Z. Geng, Z. Shao, W. Lu, F. Xie, H. Xiao, X. Qin, and B. Yi, *Appl. Catal. B*, 2013, 132, 183-194.
16. G. X.Wang, H. Wu, D. Wexler, H. K. Liu, and O. Savadogo,*J. Alloys. Compd.*, 2010, 503,1-4.
17. H. Zhu, X. W. Li, and F. H. Wang, *Int. J. Hydrogen Energy*, 2011, 36, 9151-9154.
18. I. Razack, N. Sujatha, N. Rajalakshmi, and S. Ramaprabhu, *Int. J. Hydrogen Energy*, 2009, 34, 6371-6376.
19. Y. Liang, Y.G. Li, H. Wang, J. Zhou， J. Wang, T. Regier, *Nat. Mater.*, 2011, 10, 780-786.
20. C. Niancai, R. Kutz, C. Kemna, and A. Wieckowski, *J. Electroanal. Chem.*, 2013, 705, 8-12.
21. S. Mukerjee, R. Zeis, S. Parres-Esclapez, M. Illán-Gómez, and A. Bueno-López, *Appl. Catal.A*, 2010, 381, 54-65.
22. H. Wang, F. Peng, J. Liang, H. Yu, and J. Yang, *Langmuir*, 2009, 25, 7711.
23. O. Yoshiro, A. Ishihara, K. Matsuzawa, S. Mitsushima, K. Ota, M. Matsumoto, and H. Imai, *Electrochim. Acta.*, 2012, 68, 192-197.
24. S. Sangaraju and A. Gedanken, *J. Phys. Chem.B*, 2006, 110, 24486-24491.
25. S. P .Yu, Q. B. Liu, W. S. Yang, K. F. Han, Z. M. Wang and H. Zhu.*Electrochim. Acta.*, 2013, 94, 245-251.
26. D. Meiling, M. Hou, D. Liang, W. Lu, Z. Shao, and B. Yi, *Electrochim. Acta.*, 2013, 92, 468-473.
27. A, Zaenal, M. Suzuki, J. Masud, T. Okajima, and T. Ohsaka, *J. Phys. Chem.B*, 2011, 115, 25557-25567.
28. N.Elezovic, M. Babic, R. Radmilovic, M. Vracar, and V. Krstajic, *Electrochim. Acta.*, 2009, 54, 2404-2409.
29. C. Wei, N.David, and C. Shaowei, *J. Power Sources*, 2010, 195, 412-418.
30. P. Divya, T. Theres, V. Parambhath, R. Natarajan, and R. Sundara, *Int.J. Hydrogen Energy*, 2013, 38, 6460-6468.
31. Z. Dandan,Z, Yongqing, Z, Xuan, X. Cailing, Y. Peng, Li. Hulin, and Z. Yang,*Mater. Lett.*, 2013, 107, 115-118.

32. T. Fei, S. Santhanagopalan, W. Ying, and D. Meng, *J. Alloys Compd.*, 2010, 499, 259-264.
33. L. Jang-Soo, G. Park, H. Lee, S. Kim, C. Ruiguo, L. Meilin, and C. Jaephil, *Nano. Lett.*, 2011, 11, 5362-5366.
34. F.Cheng, J. Shen, W. Ji, Z. Tao, and J. Chen, *ACS. Appl. Mater. Interfaces*, 2009, 1, 460-466.
35. W. Xiao, W. Deli, and X. Wen, *J. Phys. Chem. C*, 2009, 114, 1694-1700.
36. S. Dawei, A. Hyo-Jun, and W. Guoxiu, *J. Mater. Chem. A*, 2013, 1, 4845.
37. S. P .Yu, Q. Lou, R. T. Liu, K. F. Han, Z. M. Wang, and H. Zhu, *Acta Chimi. Sin.*,2012, 70, 2359.
38. R.Valim, M. Santos, V. Lanza, S. Machado, B. Lima, and L. Calegaro, *Electrochim. Acta.*, 2012, 85, 423-431.
39. L. Y.Chen, , J. L. Kang, Y. Hou, P. Liu, T. Fujita, A. Hirata, and M. W. Chen, *J. Mater. Chem. A*, 2013, 1, 9202.
40. S. P .Yu, Q. Lou, K. F. Han, Z. M. Wang, and H. Zhu,*Int. J. Hydrogen Energy*, 2012, 37, 13365-13370.
41. H. F. Xu, M. F. Zhang, andQ. Q. Gan,*Electrochemistry*, 2007, 13, 316-319
42. K. G. Nishanth, P. Sridhar, and S. Pitchumani, *Electrochem. commun.*, 2011, 13, 1465-1468.
43. J. L.Reyes-Rodríguez, F. Godínez-Salomón, M. A. Leyva, and O. Solorza-Feria,*Int. J. Hydrogen Energy*, 2013, 38, 12634-12639.
44. F. Y.Cheng, Y. Su, J. Liang, Z. L. Tao, and J. Chen, *Chem. Mater.*, 2009, 22, 898-905.
45. M. S. Hossain, D. Tryk and E. Yeager,*Electrochim. Acta.*, 1989, 34, 1733-1737
46. E. Yeager,*J. Mol. Catal.*, 1986, 38, 5-25.
47. E. Yeager,*Electrochim. Acta.*, 1984, 29, 1527-1537.
48. Z. Dandan, Y. Zhao, X. Zhang, C. Xu, Yong Peng, H. Li, and Z. Yang, *Mater Lett*, 2013. 107,115-118.